# Magneto-optical properties of nanocrystals: Zeeman splitting

S. J. Prado,[1,*] C. Trallero-Giner,[2] A. M. Alcalde,[1] V. López-Richard,[3] and G. E. Marques[1]
[1]*Departamento de Física, UFSCar, Caixa Postal 676, 13565-905 São Carlos SP, Brazil*
[2]*Departament of Theoretical Physics, Havana University, Vedado 10400, Cuba*
[3]*Instituto de Física de São Carlos, USP, 13560-970, São Carlos SP, Brazil*
(Received 11 October 2002; revised manuscript received 9 January 2003; published 8 April 2003)

We discuss different aspects of the Zeeman splitting in optical properties of II-VI spherical quantum dots in presence of a external magnetic field *B*. A systematic study of the energy eigenvalues, wave functions, and their dominant symmetries within the $8\times 8$ $\mathbf{k}\cdot\mathbf{p}$ Kane-Weiler formalism, allowing the inclusion of the conduction-valence-band coupling, nonparabolicity, and mixing of the electronic and spin states, is presented. The analysis of symmetries inherent in the $\mathbf{k}\cdot\mathbf{p}$ Hamiltonian leads to sets of basis functions that can be separated into two independent Hilbert subspaces. The linear and quadratic Zeeman splitting in the quantum dot have been studied in the strong confinement regime. A detailed discussion of the symmetries associated with the electronic levels and the magneto-optical selection rules for interband transitions are derived. We also calculated the optical oscillator strengths and their corresponding magnetoabsorption coefficient for Faraday and Voigt configurations. It shows that the effective Landé *g* factor, obtained theoretically, and diamagnetic shift can be tested experimentally by complementary optical spectra measured in Faraday and Voigt geometries.

DOI: 10.1103/PhysRevB.67.165306 PACS number(s): 73.21.La, 78.67.Hc

## I. INTRODUCTION

Much theoretical and experimental effort has lately been dedicated to understand as well as explore the physical properties of the semiconductor nanostructures in presence of external magnetic fields, **B**. The ability to manipulate and control spin states as well as to modulate the *g* factor is, at the present moment, of fundamental importance in the study of electronic systems with potential applications in spintronic computation, quantum communication, and quantum computation. Semiconductor quantum dots of diverse geometries have been targeted as serious candidates for the implementation of these new devices. Many aspects of the effects of the magnetic fields on the optic properties in semiconductor quantum dots still remain under discussion, especially the effects of the quantum confinement on magnitudes such as the Landé *g* factor or the oscillator strengths for transitions with or without spin inversion. In this direction, the spherical quantum dots (SQD's) grown in a host matrix, especially in the strong confinement regime, provide an ideal environment for the study of the confinement effects. The starting point for a serious study of any optical or spintronic properties is the rigorous determination of the energy eigenvalues and wave functions. The strong spatial localization generated by the confinement potential and mainly the effects of the broken symmetries induced by the external magnetic field are two aspects that should be studied when considering a realistic model of quantum dots.

Several works have been devoted to studying the effects of the magnetic field on the electronic conduction band within the simple parabolic model. Also, quantum dots with cylindrical geometry in presence of magnetic fields **B** have been analyzed.[1] The magnetic-field effects in quantum dots have been studied experimentally[2–5] and theoretically.[6–8] Interesting results were obtained in the determination of several optical properties such as exciton fine structure, Zeeman effect, and Landau-level formation. Several types of theoretical approaches have been generally used to solve the eigenvalue problem in a quantum dot in presence of an applied magnetic field. Techniques that are based on exact diagonalization[6] demand many computational resources and procedures of fast convergence such as the boundary element method[9] and can become formidably complex if coupling effects between bands are included. The $\mathbf{k}\cdot\mathbf{p}$ method allows to describe, in a precise manner, the most important facts that define the electronic structure of a quantum dot in presence of an external magnetic field. This method has been generally applied to two-dimensional III-V quantum dots with parabolic confinement. For this kind of geometry, the problem has an exact parabolic solution, thus a well-defined basis set of functions can be used to diagonalize the $\mathbf{k}\cdot\mathbf{p}$ Hamiltonian. Kotlyar *et al.*,[8] for example, have calculated the hole states in the valence band using a six-band Hamiltonian, and Darnhofer and Rössler[10] have used an eight-band formalism to include the coupling between valence and conduction bands and the effects of the spin-orbit coupling. The diagonal parabolic problem is that SQD's do not possess a separable solution, since the magnetic effective confining potential cannot be expressed as a sum of potentials with independent variables. This is so because the diamagnetic term, proportional to the square of the magnetic field, mixes the spatial variables. Thus, it is not a trivial task to define a basis set that allows the diagonalization of the $\mathbf{k}\cdot\mathbf{p}$ Hamiltonian for an arbitrary magnitude of magnetic field. The range of the magnetic and spatial potentials defined by the cyclotron length $l_B=\sqrt{\hbar c/eB}$ and the dot radius *R*, respectively, allows us to distinguish two opposite regimes for the study of the electronic structure: (i) $l_B>R$ is a regime where the magnetic field plays the role of a weak perturbation to the system. The dominant contribution comes from the spatial confinement, with the magnetic field breaking the Kramer's degeneracy. (ii) $l_B<R$ is a regime of intense magnetic fields where the cylindrical component of the magnetic confinement potential becomes the most significative and dominant effect that leads to the formation of Landau levels. As we discuss below, un-

 ©2003 The American Physical Society

der the condition $l_B > R$, the eigenfunctions at $B=0$ represent an appropriate set of wave functions to diagonalize the $\mathbf{k}\cdot\mathbf{p}$ Hamiltonian including the magnetic-field effect. The condition $l_B > R$ is particularly interesting, since the Zeeman splitting and spin-flip transitions are revealed. Also, calculation and experimental determination of the $g$ factor have been performed under this particular magnetic-field region. For materials and the dot geometry considered in the present work, the formation of Landau levels only occurs at magnetic-field intensities near to or greater than 60 T. This statement was verified by means of the calculation of electron energies within the strong perturbation theory.[11,12] Recently, Planelles *et al.*[13] presented a calculation of the electronic structure of SQD's in presence of magnetic fields based on the four-band $\mathbf{k}\cdot\mathbf{p}$ but neglected spin splitting effects. In fact, the use of this method allows to describe the mixture of $lh$ and $hh$ states. Nevertheless, due to the limited band model used by these authors they were not able to discussion important effects such as the spin-flip and spin splitting mixing of spin states, nonparabolicity, and the effects of the involved symmetries due to the interaction between conduction, valence, and split-off bands. In order to achieve a better quantitative description of the magnetoprofile for electrons and holes, spatial quantum confinement, the electronic $g$ factor, and magneto-optical properties of nanocrystals, in this work we explore all the inherent power of the $8\times 8$ $\mathbf{k}\cdot\mathbf{p}$ Kane-Weiler Hamiltonian to rigorously determine the electronic structure in a single CdTe SQD in presence of an external magnetic field. On this basis, we are be able to discuss and determine many relevant properties of the electronic states and magneto-optical properties valid in the regime $l_B > R$. The actual Hamiltonian model takes into account the coupling between conduction and valence bands, the contribution of the remote bands, the nonparabolicity effects, and the mixing at the valence bands. In Sec. II of this paper we extend the $8\times 8$ $\mathbf{k}\cdot\mathbf{p}$ Hamiltonian to a nanocrystal with spherical symmetry in an external magnetic field according to its inherent symmetry, and for the case of $l_B > R$, we provide an appropriate basis set and the Hilbert subspaces to describe the SQD electronic structure. Also, magneto-optical selection rules for Faraday and Voigt geometries are derived. Section III is devoted to discussing the size dependence and magnetic-field effect on electronic states and on optical spectra. Finally, we sum our results in Sec. IV.

## II. THEORY

Following the effective-mass approximation, we describe a carrier in the presence of an external magnetic field $\mathbf{B}=(0,\ 0,\ B)$ and a confinement potential $V$ from the solutions of the Schrödinger equation $H_{k\cdot p}\psi = E\psi$ for the eight-component spinor $\psi$. The magnetic-field effects can be included after replacing $\mathbf{p}$ with $\mathbf{p}+(e/c)\mathbf{A}$. Here $\mathbf{p}$ represents the momentum operator and $\mathbf{A}=\frac{1}{2}Br\sin\theta(-\sin\phi\hat{\mathbf{e}}_x + \cos\phi\hat{\mathbf{e}}_y)$ is the vector potential for the uniform magnetic field written in the symmetric gauge. We have chosen to use the complete $8\times 8$ $\mathbf{k}\cdot\mathbf{p}$ Kane-Weiler model,[14–17] which takes into account the known interactions between states in the $\Gamma_6$, $\Gamma_8$, and $\Gamma_7$ bands exactly, and to consider the contributions of the remote bands. The $\mathbf{k}\cdot\mathbf{p}$ Hamiltonian is reported in Ref. 17 and its matrix elements taking into account the magnetic-field effects are defined explicitly in the Appendix A. Under the condition $l_B > R$ some characteristics of our approach should be specifically pointed out. (i) The inherent symmetry existing in the $\mathbf{k}\cdot\mathbf{p}$ Hamiltonian allows the separation of the Hilbert space into two orthogonal subspaces. We expand the eight-component spinor wave functions in each Hilbert subspace, in terms of the exact solutions of the diagonal operators for each carrier type at $B=0$. In general, each component of the spinor has the form $f^M_{n,L}(r,\Omega) = A_{n,L}j_L(\mu^L_n r/R)Y^M_L(\Omega)$,[18] with a special sequence of parity dictated from the inherent symmetry of $H_{k\cdot p}$. Here the $z$ component of the orbital angular momentum $L$ ($L_z = \hbar M$, $M=0,\ \pm 1, \ldots$) remains a good quantum number, while is not possible to find states with well-defined spin and orbital quantum numbers, since these states are mixed by the effects of the magnetic field and the interband couplings. (ii) The wave functions $\psi_{\mathrm{I(II)}}$ for subspaces I and II, fulfilling the boundary condition $\psi_{\mathrm{I(II)}}(R)=0$,[19] can be written as a linear combination of the envelopes $f^M_{n,L}(r,\Omega)$ and the eight Bloch functions at the $\Gamma$ point, as

$$|\psi^M_{\mathrm{I(II)}}\rangle = \sum_n \sum_{L\geqslant|M|}^{\infty} \begin{pmatrix} f^M_{n,2L(2L+1)}|e^+\rangle \\ f^{M-1}_{n,2L+1(2L)}|hh^+\rangle \\ f^M_{n,2L+1(2L)}|lh^+\rangle \\ f^M_{n,2L+1(2L)}|so^+\rangle \\ f^{M+1}_{n,2L(2L+1)}|e^-\rangle \\ f^{M+2}_{n,2L+1(2L)}|hh^-\rangle \\ f^{M+1}_{n,2L+1(2L)}|lh^-\rangle \\ f^{M+1}_{n,2L+1(2L)}|so^-\rangle \end{pmatrix}. \qquad (1)$$

It is important to note that the spinors $|\psi^M_{\mathrm{I(II)}}\rangle$ do not present a defined parity ($\pm$), as assumed in Ref. 20 but, instead, the special mixture as indicated above. Within the $8\times 8$ $\mathbf{k}\cdot\mathbf{p}$ Hamiltonian the states with different symmetries are coupled even at $B=0$. Nevertheless, by neglecting only the warping term, proportional to $\mu=(\gamma_2-\gamma_3)/2$, the space of solutions of the Kane-Weiler Hamiltonian in spherical coordinates can be separated into the two independent subspaces with the specified values for the angular quantum number $L$ in each Bloch state. At $B\neq 0$ the only good quantum number $(M+J_z)$ [$J_z$ being the $z$ component of the Bloch angular momentum $J$ (Ref. 17)] along the field is preserved. Moreover, the applied field $B$ does not modify the boundary conditions over the radial part of the function $f^M_{n,L}(r,\Omega)$ and the above spinors (1) constitute a complete basis set of orthonormal functions for the effective $8\times 8$ $\mathbf{k}\cdot\mathbf{p}$ Hamiltonian in each subspace, a very useful tool for the case in which $l_B \geqslant R$. (iii) In our matrix diagonalization scheme we have ordered the envelope functions $f^M_{n,L}(r,\Omega)$ for each carrier set ($e^{\pm}$, $hh^{\pm}$, $lh^{\pm}$, and $so^{\pm}$, following the notation of Ref. 17) for increasing values of the energy $E_i$,

$i=1 \ldots N_0$. Therefore, we can replace the sum $\Sigma_{n,L}$, in the expansion (1), by $\Sigma_{E_i}$ with the magnetic index $M$ fixed. This procedure permits us to select only the most important contributions for the formation of a given state and obtaining a significant gain in computational efficiency, since we must diagonalize matrices much smaller than the ones normally used in standard procedures. Hence, the results we present can been achieved using matrices of size of $8N_0 \times 8N_0$, with $N_0 \leqslant 30$. The results are fully converged to good numerical accuracy. (iv) Although the confinement potential is spherical, the $\mathbf{k}\cdot\mathbf{p}$ Hamiltonian is essentially of cylindrical symmetry, since we allow the Luttinger parameters $\gamma_2 \neq \gamma_3$ everywhere but the terms proportional to the warping term $\mu$ are equal to zero. The presence of these cylindrical components in the Hamiltonian modifies the effective spherical confinement potential that acts on the carriers. The theory considered here takes into account the complex interplay between these superimposed symmetries plus the conduction- and valence-band coupling in order to describe the Zeeman splitting of electronic states.

The optical transition probability is proportional to the matrix element of the crystal-radiation field interaction $\langle \psi_{e,j}|\hat{\mathbf{e}}\cdot\hat{\mathbf{P}}|\psi_{h,j'}\rangle$, $j,j'=\mathrm{I}, \mathrm{II}$, where $\hat{\mathbf{e}}$ is the light polarization vector and $\hat{\mathbf{P}}$ is the momentum operator. Using Eq. (1) the above matrix element can be written as

$$\langle \psi^{M_e}_{e,j}|\hat{\mathbf{e}}\cdot\hat{\mathbf{P}}|\psi^{M_h}_{h,j'}\rangle = \sum_{\alpha,\alpha'} \langle f^{M_e}_{e,\alpha}|f^{M_h}_{h,\alpha'}\rangle\langle u_\alpha|\hat{\mathbf{e}}\cdot\hat{\mathbf{P}}|u_{\alpha'}\rangle + \langle u_\alpha|u_{\alpha'}\rangle\langle f^{M_e}_{e,\alpha}|\hat{\mathbf{e}}\cdot\hat{\mathbf{P}}|f^{M_h}_{h,\alpha'}\rangle. \quad (2)$$

Here the states of the conduction (valence) band are labeled $f^{M_e}_{e,\alpha}$ ($f^{M_h}_{h,\alpha}$), with $\alpha$ enumerating the corresponding quantum numbers $n$, $L$ and the periodic Bloch functions at the $\Gamma$ point of the Brillouin zone, $|u_\alpha\rangle = |J,\ J_z\rangle$, in the sequence followed in the Eq. (1) (see the Appendix).

For interband transitions, only the first term in Eq. (2) contributes to the overlap integral, which can be separated into integrations over the fast oscillating Bloch part that determine the interband selection rules, and integrations over the envelope part that determine the intensities of the transitions proportional to the oscillator strengths. The integrations of the Bloch function part result in the size-independent dipole matrix elements that will be named $\Pi_{\alpha,\alpha'} = \langle u_\alpha|\hat{\mathbf{e}}\cdot\hat{\mathbf{P}}|u_{\alpha'}\rangle$. The complete set of selection rules are obtained from the nonvanishing products of the matrix elements $I_{e,h}\delta_{L_e,L_h}\Pi_{\alpha,\alpha'}$, where $I_{e,h} = \langle f_{e,\alpha}|f_{h,\alpha'}\rangle$ are the envelope overlap integrals.

The allowed transitions between the two separated Hilbert subspaces, as described by the spinors (1), are determined from the angular dependence of the wave functions. By taking the magnetic field $\mathbf{B}$ as the proper $z$ quantization axis for the Bloch functions $|u_\alpha\rangle$ we can determinate the selection rules for two independent configurations: Faraday, when the wave vector of the incident light $\hat{\boldsymbol{\kappa}} \| \mathbf{B} \| \hat{\mathbf{z}}$, and the Voigt if $\hat{\boldsymbol{\kappa}} \perp \mathbf{B} \| \hat{\mathbf{z}}$. In Faraday geometry and incident light with left circular polarization $\hat{\mathbf{e}}^- = (\hat{\mathbf{e}}_x - i\hat{\mathbf{e}}_y)/\sqrt{2}$, the dipole matrix $\Pi$ gives us

$$\Pi^- = \frac{iP}{\sqrt{3}} \begin{bmatrix} 0 & -\sqrt{3} & 0 & 0 & 0 & 0 & 0 & 0 \\ 0 & 0 & 0 & 0 & 0 & 0 & 0 & 0 \\ 0 & 0 & 0 & 0 & 0 & 0 & 0 & 0 \\ 0 & 0 & 0 & 0 & 0 & 0 & 0 & 0 \\ 0 & 0 & 1 & \sqrt{2} & 0 & 0 & 0 & 0 \\ 0 & 0 & 0 & 0 & -\sqrt{3} & 0 & 0 & 0 \\ -1 & 0 & 0 & 0 & 0 & 0 & 0 & 0 \\ -\sqrt{2} & 0 & 0 & 0 & 0 & 0 & 0 & 0 \end{bmatrix}, \quad (3)$$

where $iP = i\langle S|P_x|X\rangle$ is proportional to the Kane coupling parameter, $P_0$. The corresponding matrix interaction for right circular polarization $\hat{\mathbf{e}}^+ = (\hat{\mathbf{e}}_x + i\hat{\mathbf{e}}_y)/\sqrt{2}$ is obtained from the Hermitian adjoint $\Pi^+ = -[\Pi^-]^\dagger$. In the case of Voigt geometry, the optical processes with linear polarization $\hat{\mathbf{e}} = \hat{\mathbf{e}}_z$ are represented through the following matrix interaction:

$$\Pi^z = \frac{iP}{\sqrt{3}} \begin{bmatrix} 0 & 0 & \sqrt{2} & -1 & 0 & 0 & 0 & 0 \\ 0 & 0 & 0 & 0 & 0 & 0 & 0 & 0 \\ \sqrt{2} & 0 & 0 & 0 & 0 & 0 & 0 & 0 \\ -1 & 0 & 0 & 0 & 0 & 0 & 0 & 0 \\ 0 & 0 & 0 & 0 & 0 & 0 & \sqrt{2} & -1 \\ 0 & 0 & 0 & 0 & 0 & 0 & 0 & 0 \\ 0 & 0 & 0 & 0 & \sqrt{2} & 0 & 0 & 0 \\ 0 & 0 & 0 & 0 & -1 & 0 & 0 & 0 \end{bmatrix}. \quad (4)$$

On the grounds of Eqs. (3) and (4), the corresponding selection rules for each optical transition in any polarization can be precisely obtained. It can be seen, according to the structure of both of the obtained Hilbert subspaces described by the wave functions $\psi^M_{\mathrm{I(II)}}$ and the dipole matrix elements (3) and (4), that the interband optical transitions between the same Hilbert subspace I (II) are forbidden in both studied geometries. Thus, for circular $\hat{\mathbf{e}}^\pm$ (Faraday $\sigma^\pm$ geometry) and linear $\hat{\mathbf{e}}_z$ (Voigt $\pi^z$ geometry) polarizations, only the optical transitions between initial $M_i(H_i)$ and final $M_f(H_f)$ levels belonging to different Hilbert subspaces $H=\mathrm{I}, \mathrm{II}$ are allowed. Selection rules do not allow interband transition from the same Hilbert subspaces (I→I or II→II), because of the different symmetries of the electron and hole angular momenta. Moreover, for the magnetic quantum numbers we have $\Delta M = \pm 1$ and $\Delta M = 0$ for the Faraday and Voigt configurations, respectively.

In the framework of the confined potential model here used, the matrix element (2) is reduced to (for left circular polarization)

$$\langle \psi_{e,\mathrm{I}}^{M_e} | \hat{\mathbf{e}}^{-} \cdot \hat{\mathbf{P}} | \psi_{h,\mathrm{II}}^{M_h} \rangle = iP \mathcal{F}_{N_e,M_e}^{N_h,M_h}(\mathrm{I,II})\, \delta_{M_e,M_h \pm 1}, \quad (5)$$

where

$$\mathcal{F}_{N_e,M_e}^{N_h,M_h}(\mathrm{I,II}) = \sum_{n,L \geqslant |M|} \left\{ -A_{n,\beta}^{e^{\pm}} A_{n,\beta}^{hh^{\pm}} \pm \frac{1}{\sqrt{3}} A_{n,\beta}^{e^{\mp}} \left[ A_{n,\beta}^{lh^{\pm}} + \frac{1}{\sqrt{2}} A_{n,\beta}^{so^{\pm}} \right] \right\}, \quad (6)$$

with $\beta = 2L + 1/2 \mp 1/2$. In the same way the I→ II transition is obtained by interchanging $2L+1/2 \mp 1/2$ by $2L+1/2 \pm 1/2$. If we consider right circular polarization we solely have to substitute the signs $(\pm)$ in Eqs. (5) and (6) by $(\mp)$ and vice versa.

In order to discuss the magneto-optical absorption spectra, the interband oscillator strength $|\mathcal{F}|^2$ between single electron $(N_e, M_e)$ and hole $(N_h, M_h)$ states has to be evaluated in detail. The absorption coefficient can be cast as

$$\alpha(\hat{\mathbf{e}}^{-}, \omega) = \alpha_0 \sum_{N_e,N_h,M} \frac{\Gamma}{\pi} \times \left\{ \frac{|\mathcal{F}_{N_e,M}^{N_h,M\pm1}(\mathrm{I,II})|^2}{(E_{N_e,M}(\mathrm{I}) - E_{N_h,M\pm1}(\mathrm{II}) - \hbar\omega)^2 + \Gamma^2} + \frac{|\mathcal{F}_{N_e,M}^{N_h,M\mp1}(\mathrm{II,I})|^2}{(E_{N_e,M}(\mathrm{II}) - E_{N_h,M\mp1}(\mathrm{I}) - \hbar\omega)^2 + \Gamma^2} \right\}. \quad (7)$$

In the above equation we neglected the effects of nonhomogeneous broadening, which arise from the dot size fluctuation in a sample, and a constant broadening $\Gamma$ is assumed for all kinds of transitions; $\alpha_0$ is a constant and $\omega$ is the incident light frequency. A similar expression can be obtained when we consider Voigt geometry, that is

$$\alpha(\hat{\mathbf{e}}_z, \omega) = \alpha_0 \sum_{N_e,N_h,M} \frac{\Gamma}{\pi} \times \left\{ \frac{|\mathcal{V}_{N_e,M}^{N_h,M}(\mathrm{I,II})|^2}{(E_{N_e,M}(\mathrm{I}) - E_{N_h,M}(\mathrm{II}) - \hbar\omega)^2 + \Gamma^2} + \frac{|\mathcal{V}_{N_e,M}^{N_h,M}(\mathrm{II,I})|^2}{(E_{N_e,M}(\mathrm{II}) - E_{N_h,M}(\mathrm{I}) - \hbar\omega)^2 + \Gamma^2} \right\}, \quad (8)$$

where

$$\mathcal{V}_{N_e,M}^{N_h,M}(\mathrm{I,II}) = 2 \sum_{n,L \geqslant |M|} \{ \sqrt{2} A_{n,\beta}^{e^{\pm}} A_{n,\beta}^{lh^{\pm}} - A_{n,\beta}^{e^{\pm}} A_{n,\beta}^{so^{\pm}} \}, \quad (9)$$

and for the II→I we must interchange the index $(\pm)$ by $(\mp)$ in the above equations.

## III. RESULTS

The parameters for CdTe (Ref. 20) used in this calculation are the energy band gap $E_g = 1.6069$ eV and the spin-orbit energy $\Delta_0 = 0.953$ eV. The Luttinger parameters are $\gamma_1^L = 5.37$, $\gamma_2^L = 1.67$, and $\gamma_3^L = 1.98$; the nonparabolicity parameter for the conduction band is $(1+2F) = 1.24$; and the second-order magnetic parameters are $N_w = 0$, $\kappa = 1.267$, and $q = -1.099$ (see the Appendix for a brief discussion about the meaning of the second-order parameters). The electron effective mass is $m_e = 0.091 m_0$ and the Kane parameter is $E_p = 17.9$ eV. For all calculated optical spectra in this work, we have used a unique value for the homogeneous electronic broadening, $\Gamma = 1.0$ meV, of the optical transitions.

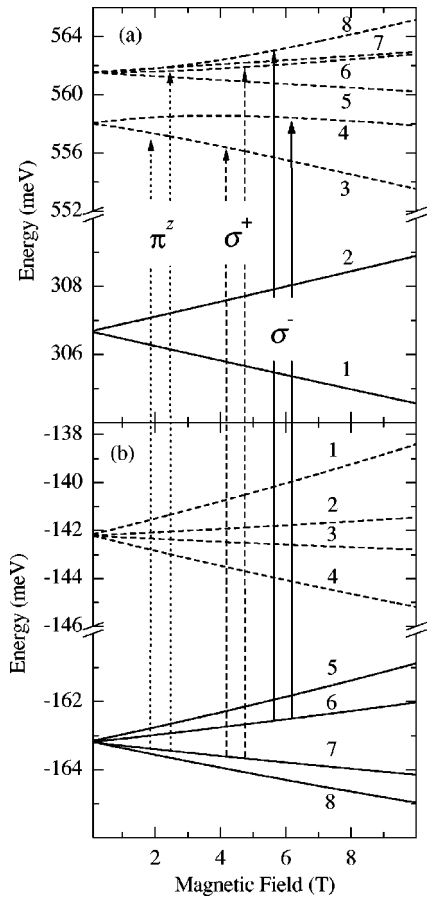


FIG. 1. Electron and hole energy spectra of a 30-Å CdTe SQD, plotted as a function of magnetic field *B*. Solid (dashed) lines represent states arising from Hilbert subspace I (II). The levels have been identified considering the quantum number *M* and the energy order index *N* (see text for details). (a) Conduction band 1: ${}_{-1}e^{1\downarrow}$, 2: ${}_{0}e^{1\uparrow}$, 3: ${}_{0}e^{1\downarrow}$, 4: ${}_{-1}e^{1\uparrow}$, 5: ${}_{+1}e^{1\uparrow}$, 6: ${}_{0}e^{2\uparrow}$, 7: ${}_{-2}e^{1\downarrow}$, and 8: ${}_{-1}e^{2\downarrow}$; (b) valence band 1: ${}_{+1}hh^{1\uparrow}$, 2: ${}_{0}lh^{1\uparrow}$, 3: ${}_{-1}lh^{1\downarrow}$, 4: ${}_{-2}hh^{1\downarrow}$, 5: ${}_{+1}hh^{2\uparrow}$, 6: ${}_{0}lh^{1\downarrow}$, 7: ${}_{-1}lh^{1\uparrow}$, and 8: ${}_{-2}hh^{2\downarrow}$. Several optical transitions are indicated for Faraday $(\sigma^{\pm})$ and Voigt $(\pi^z)$ geometries with $\hat{\mathbf{e}}^{\pm}$ and $\hat{\mathbf{e}}_z$ polarizations, respectively.

In Figs. 1 and 2 we show the dependence of the energy levels with the magnetic field for two SQD's with radii 30 Å and 50 Å, respectively. In Figs. 1(a) and 2(a) are displayed the electron energies and in Figs. 1(b) and 2(b) are hole energies. For a given value of magnetic field, the levels are labeled by the quantum number *M* and by the energy ordering number *N*. Additionally, we identify the levels by means

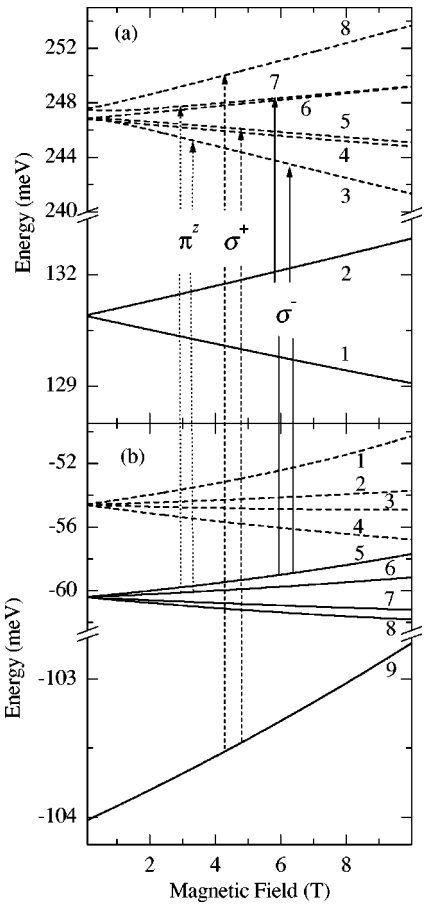


FIG. 2. The same as Fig. 1 for a 50-Å CdTe SQD. (a) Conduction band 1: ${}_{-1}e^{1\downarrow}$, 2: ${}_{0}e^{1\uparrow}$, 3: ${}_{0}e^{2\uparrow}$, 4: ${}_{+1}e^{1\uparrow}$, 5: ${}_{-1}e^{2\downarrow}$, 6: ${}_{-2}e^{1\downarrow}$, 7: ${}_{0}e^{1\downarrow}$, and 8: ${}_{-1}e^{1\uparrow}$; (b) valence band 1: ${}_{+1}hh^{1\uparrow}$, 2: ${}_{0}lh^{1\uparrow}$, 3: ${}_{-1}lh^{1\downarrow}$, 4: ${}_{-2}hh^{1\downarrow}$, 5: ${}_{+1}hh^{2\uparrow}$, 6: ${}_{0}lh^{1\downarrow}$, 7: ${}_{-1}lh^{1\uparrow}$, 8: ${}_{-2}hh^{2\downarrow}$, and 9: ${}_{-2}hh^{4\downarrow}$.

of the spin number [$s=\uparrow$ (up), $s=\downarrow$ (down)] and the carrier character. This notation is used in considering the large absolute value of the weight coefficients $A_{n,L}$ at $B=0$ for each kind of carrier. Thus, an electron level is represented as ${}_{M}e^{N\uparrow(\downarrow)}(H)$ and a heavy hole state as ${}_{M}hh^{N\uparrow(\downarrow)}(H)$, with $H$ representing the Hilbert subspace to which the carrier state belongs. The same notation is used for light ($lh$) or split-off ($so$) states and is appropriate if one looks to the form of which each state function [Eq. (1)] is written. Some important characteristics should be pointed out in the analysis of these results: (i) The linear splitting dependence on $B$ is due to the linear Zeeman effect [terms proportional to $\hbar MB$ in matrix elements (A2)] and the existence of an ''effective'' $g$ factor for electron and hole levels through the parameters $N_w$ and $\kappa$ [see the diagonal elements of the $8\times8$ Hamiltonian (A1)]. For example, in Fig. 1, the splitting of the states labeled 1, 2 in the conduction bands 1, 4 and 2, 3 for the heavy and light valence bands, respectively, are due to the spin orientation along the field $B$, i.e., the electron and hole $g$ factors. The levels 4 ($M=-1$) and 5 ($M=1$) in Fig. 1(a) represent the linear Zeeman behavior at low field ($B<2$ T) in the SQD. The same can be argued for the other states in Figs. 1 and 2 by checking the effective $g$ factor or the linear Zeeman splitting effect for each carrier in the SQD. The splitting of the lowest levels is nearly proportional to $B$ in the entire range of magnetic fields in the regime studied in this work. (ii) For both dot sizes considered, the effects of the diamagnetic contribution, proportional to $B^2$, can be clearly observed in the six excited electron levels labeled 3–8 in Figs. 1 and 2. This contribution causes deviation in the energy levels from the linear dependence on $B$, which is expected when the diamagnetic term is not included. In other II-VI nanocrystals, such as CdS SQD's, the diamagnetic effects are only observed starting from field $B\approx20$ T,[6] different from CdTe SQD's where this effect is already appreciable for fields $B\approx2$ T. Therefore, our results demonstrate that the exclusion in the Hamiltonian of the terms proportional to $B^2$ [see Eqs. (A4), (A8), and (A9) in the Appendix] is applicable only in the case of very weak fields ($B\approx1$ T for the excited states). (iii) We should pay attention to the spin splitting at $B=0.1$ T, produced by the effects of the asymmetry of inversion of the $\mathbf{k}\cdot\mathbf{p}$ Hamiltonian, and the spherical confinement effective potential. This effect can be observed, for instance, in Fig. 1(a) for levels 3-8. (iv) Another interesting characteristic that can be observed is the change in the order of the energy levels. In Fig. 1(a), for $R=30$ Å the first two excited states are identified as ${}_{0}e^{1\downarrow}$(II) and ${}_{-1}e^{1\uparrow}$(II), respectively; when the radius increases to $R=50$ Å [see Fig. 2(a)], the first two excited states are now levels ${}_{0}e^{2\uparrow}$(II) and ${}_{+1}e^{1\uparrow}$(II), respectively.

This exchange in the sequence of the energy levels can be explained by the change of identities between the states due to an admixture of wave functions when the radius $R$ is increased. At $R=30$ Å, the main weight contribution corresponds to the state ${}_{0}e^{\downarrow}$(II), while at $R=50$ Å the state ${}_{0}e^{\uparrow}$(II) is the dominant one.

Since we have been able to describe the electronic structure, our next step is to calculate the interband transition probability within the dipolar approximation by considering the different light polarizations and, according to Eqs. (6) and (9), we will determine the dependence of the magneto-optical oscillator strengths on the magnetic field. Following the adopted notation, an interband transition from the initial hole state, characterized by quantum numbers $N_i$, $M_i$, and $s_i$ to the final electron state defined by $N_f$, $M_f$, and $s_f$ is represented as ${}_{M_f}e^{N_f,s_f}(H_f)\leftarrow{}_{M_i}hh(lh,so)^{N_i,s_i}(H_i)$. Note that the index $N$ is an energy ordering index. In this calculation, we have neglected the effects of temperature by assuming that the electron and hole distribution functions are $F_c(E_c)\approx1$ and $F_v(E_v)\approx0$, respectively.

In Fig. 3 we present several calculated oscillator strengths as a function of the magnetic field, in a CdTe SQD, for the $\sigma^{\pm}$ and $\pi^z$ geometries. Figure 3(a) is for a $R=30$ Å SQD while Fig. 3(b) corresponds to $R=50$ Å. The allowed transitions included in this figures are indicated by the rows in Figs. 1 and 2. We only include the transitions that present significant variations with the magnetic field and omit those transitions that are almost field independent. The dominant transitions (not shown in Fig. 3) for $R=30$ Å and $R=50$ Å are ${}_{-1}e^{1\downarrow}$(I)$\leftarrow{}_{-2}hh^{1\downarrow}$(II) (Faraday for $\hat{\mathbf{e}}^{+}$ polarization), ${}_{0}e^{1\uparrow}$(I)$\leftarrow{}_{+1}hh^{1\uparrow}$(II) (Faraday for $\hat{\mathbf{e}}^{-}$ polarization), and

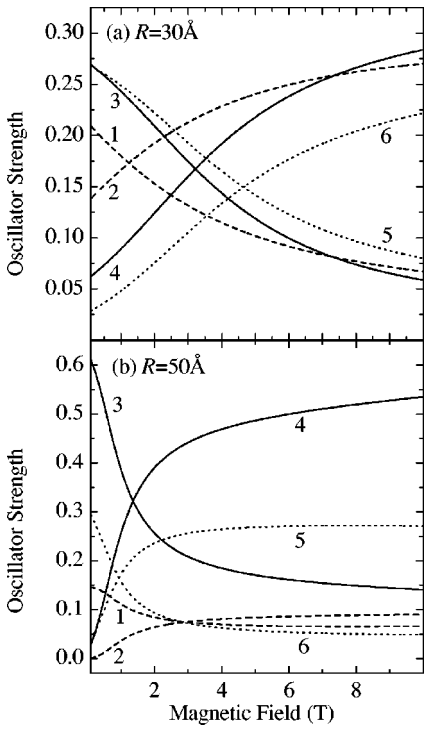


FIG. 3. Calculated magneto-optical oscillator strength as a function of the magnetic field, for (a) $R=30$ Å and (b) $R=50$ Å. Faraday geometry, $|\mathcal{F}_{N_e,M}^{N_h,M\pm1}|^2$ with the left (right) polarization, is shown by solid lines (dashed lines), while Voigt $|\mathcal{V}_{N_e,M}^{N_h,M}|^2$ geometries by dotted lines. The corresponding transitions are indicated by rows in Figs. 1 and 2.

${}_0e^{1\uparrow}(\mathrm{I})\leftarrow{}_0lh^{1\uparrow}(\mathrm{II})$ (Voigt for $\hat{\mathbf{e}}_z$ polarization).

Note from Fig. 3 that the oscillator strength present crossings at some specific values of the magnetic field (from 0.5 T to 7 T). The crossing is a direct consequence of the admixture of the electronics states according to the $8\times8$ $\mathbf{k}\cdot\mathbf{p}$ Hamiltonian and their wave functions (1). To be more specific, these crossings are directly related to the optical selection rules and the anticrossing effect observed in Figs. 1 and 2. Nearby level states in the conduction band with the same symmetry present an anticrossing at certain values of the magnetic field. The repulsion between levels with the same symmetry for a given polarization may change the so-called ''forbidden'' electron-hole transitions (parabolic approximation) into allowed ones and, at certain values of magnetic field, crossing in the oscillator strength is achieved. Hence, the ''allowed'' transition at $B=0$ diminishes its optical strength as the magnetic field increases. The variation of the spectral components in the oscillator strength, as a function of $B$, determines the behavior of the overall optical properties. For example, certain transitions can be favored by tuning an appropriate intensity of the magnetic field. Also, as in the $B=0$ case, the interband transitions are only allowed between states that come from different Hilbert subspaces. The dependence of the oscillator strength on the dot size and magnetic field enhances the capability of controlling the magneto-optic properties in SQD's. In order to study the effects of the magnetic field on the optical absorption, we show, in Fig. 4, the calculated absorption coefficient in a Faraday configuration for both analyzed polarizations. Figure 5 is devoted to the independent Voigt configuration with light polarization $\hat{\mathbf{e}}_z$. The numbers of the peaks are related to the energy fan plot shown in Fig. 1 and to the oscillator strengths allowed by the magneto-optical selection rules derived in Sec. II. At this point, we comment on the magnetoabsorption spectra and electron-hole magnetoenergy dispersion. Figure 4(a) shows the spin splitting of electron and heavy-hole ground states that can be directly measured using the complementary $\sigma^{\pm}$ geometry. In this case the energy separation is proportional to the electron–heavy-hole $g$ factor. By comparison we present in Fig. 5(a) the absorption coefficient for the same window of the laser energy and magnetic field but in a $\pi^z$ configuration. It can be seen that the spectra do not show any further structure aside from the main absorp-

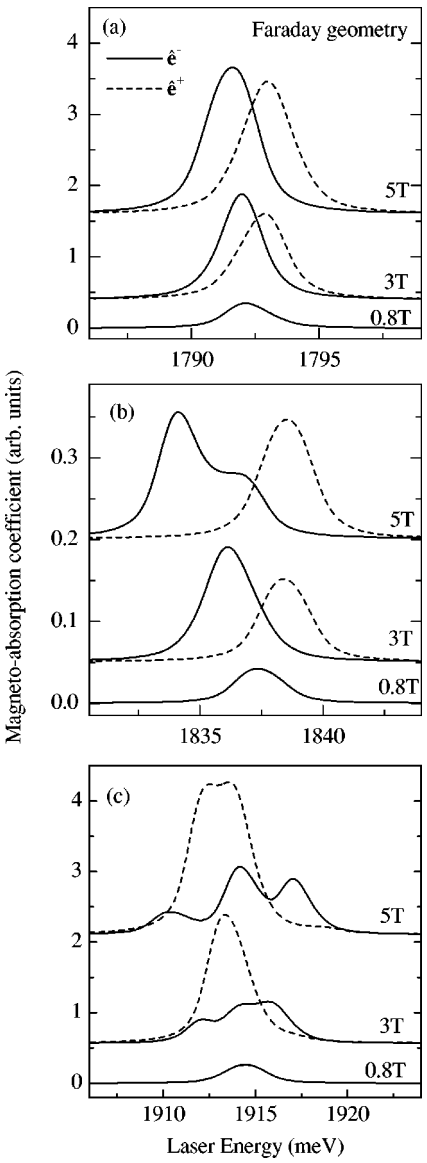


FIG. 4. Different spectra regime of the magnetoabsorption coefficient in Faraday geometry ($\mathbf{B}\|\mathbf{z}\|\hat{\kappa}$) for a 50-Å CdTe SQD, for $\hat{\mathbf{e}}^{\pm}$ polarizations.

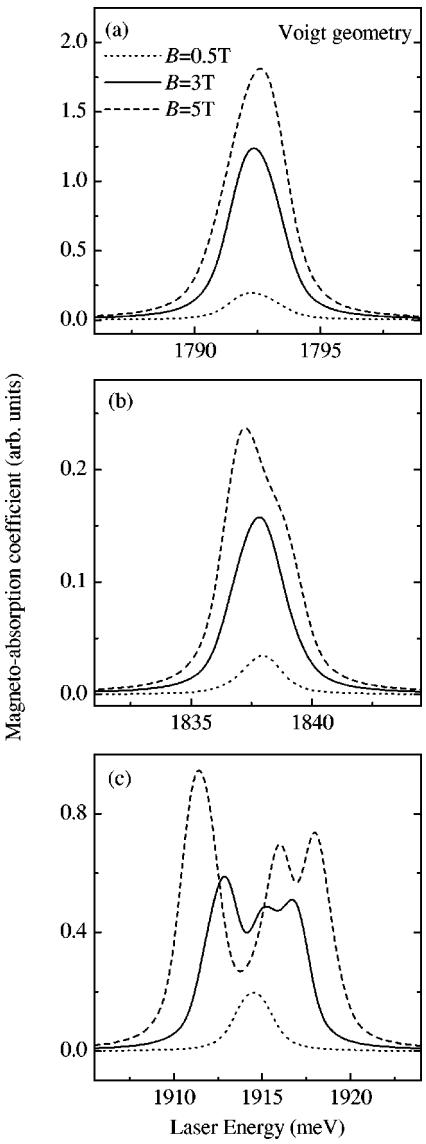


FIG. 5. The same as Fig. 4 for the Voigt geometry ($\mathbf{B}\|\mathbf{z}\perp\hat{\kappa}$) with light polarization $\hat{\mathbf{e}}_z$.

tion peaks due to an electron–light-hole transition with $\Delta M=0$. Figures 4(b) and 5(b) illustrate the behavior of the absorption coefficient in an interval of the energy where the oscillator strength is weak. These transitions correspond to $\sigma^-$: ${}_0e^{1\uparrow}(\mathrm{I})\leftarrow{}_{+1}hh^{3\uparrow}(\mathrm{II})$ and ${}_{-1}e^{1\downarrow}(\mathrm{I})\leftarrow{}_0lh^{2\uparrow}(\mathrm{II})$; $\sigma^+$: ${}_{-1}e^{1\downarrow}(\mathrm{I})\leftarrow{}_{-2}hh^{3\downarrow}(\mathrm{II})$ and ${}_0e^{1\uparrow}(\mathrm{I})\leftarrow{}_{-1}lh^{2\downarrow}(\mathrm{II})$; and $\pi^z$: ${}_0e^{1\uparrow}(\mathrm{I})\leftarrow{}_0lh^{2\uparrow}(\mathrm{II})$ and ${}_{-1}e^{1\downarrow}(\mathrm{I})\leftarrow{}_{-1}lh^{2\downarrow}(\mathrm{II})$. Figures 4(c) and 5(c) were calculated for those intensities of magnetic field and laser energy where the oscillator strength for two different transitions presents a crossing point following the results of Fig. 3. The peaks shown in these figures are related to the electron-hole transitions indicated in Fig. 2 as a function of the applied magnetic field.

A fundamental characteristic of these absorption profiles, contrary to the case $B=0$, is the linear and quadratic Zeeman splitting observed for those two independent polarizations. According to the magneto-optical selection rules described in Sec. II, the incident light in $\sigma^+$ and $\sigma^-$ geometries excites independent electronic states. In the free magnetic-field case, the shape of the absorption profile for $\sigma^+$ is exactly identical to the $\sigma^-$ configuration. This fact is a consequence of the spatial symmetry of the problem which guarantees that, in the absence of magnetic field, the energy levels are degenerate with respect to quantum number $M$. The magnetic field breaks the degeneracy and the linear and quadratic Zeeman magnetoabsorption take place, as can be clearly seen in Fig. 2 for the electron-hole transitions under consideration. Notice that the intensity of the peaks in Figs. 4(c) and 5(c) change strongly when the magnetic field is varied, and small changes in the value of the magnetic field can favor certain transitions, such as in the electron-hole transition 4 (2) for the $\sigma^-$ ($\sigma^+$) geometry or the electron-hole transition 5 for the $\pi^z$ configuration (see Fig. 3). In the latter case, changes as large as one order of magnitude in the peak intensity can be observed. On another hand, the broken $M$ degeneracy by the field induces a shift in the peaks toward higher or lower energies, as can be expected. This effect is obviously independent of the light polarization and only depends on the transition energy behavior. As can be extracted from a quick analysis of Figs. 2 and 3, the transitions 1, 3, and 5 should present a redshift in the spectrum when the magnetic field increases, together with the linear and quadratic Zeeman effects. We can observe that several transitions deviate from the typical quadratic Zeeman behavior, indicating a more complex law of the electronic fan plot with respect to the field $B$. The wide variety of transitions excited by light with different magneto-optical configurations opens a large possibility of creating elaborate experimental setups that allow to measure parameters such as the electronic and electron-hole pair $g$ factors and Luttinger parameters, and to studying their dependencies on dot size, for a given material.

## IV. CONCLUSION

We performed a theoretical study of the influence of an external magnetic field and quantum size effects in spherical nanocrystals, within the framework of the $8\times8$ $\mathbf{k}\cdot\mathbf{p}$ multiband effective-mass approximation, with the explicit inclusion of couplings between the conduction and valence bands, nonparabolicity, and band mixing. We have shown that the magnetic energy levels can be studied into two independent Hilbert subspaces. The linear and quadratic Zeeman effects and the spin splitting of the electronic carriers are obtained for relatively low magnetic fields in the case of a CdTe SQD. The concurrence of the multiband model, the spherical confinement, and the field have indicated nonlinear and nonquadratic behavior of the Zeeman splitting in the electronic magnetic fan plot (see Figs. 1 and 2). The linear Zeeman splitting is clearly obtained for a relatively ''low field,'' depending on the particular state and carrier under consideration. The interband magneto-optical transitions are only allowed between different Hilbert subspaces in Faraday and Voigt configurations.

We have predicted that particular optical configurations can be useful for extracting information from the optical spectra such as magnetoabsorption or magnetoluminescence measurements. We derived the magneto-optical selection

rules for two independent configurations (Faraday and Voigt) allowing the possibility of a direct evaluation, from the experimental point of view, of important nanocrystal parameters such as the electron-hole $g$ factor, diamagnetic coefficient, effective masses, and Luttinger parameters. In Faraday geometry the shift of the electron-hole energy optical transitions, $\Delta E_{M,N}=E_{M,N}(\sigma^+)-E_{M,N}(\sigma^-)=g_{e-h}\mu_B B$ ($\mu_B$ is the Bohr magneton), due two independent $\hat{\mathbf{e}}^{\pm}$ polarizations, directly give us the value of the $g$ factor. By using Voigt geometry one can follow the magnetic-field evolution of a desired electron-hole transition, $E_{M,N}(\pi^z)$, and, therefore, measure the linear or quadratic Zeeman effects for an appropriate chosen magnetic field. In the latter case the diamagnetic shift of the SQD is revealed. Finally, the calculation performed here can be applied to other II-VI or III-V nanocrystal compounds where experimental values of the magnetic-field evolution of the electron-hole states together with the theoretical predictions could provide available tools for determining nanostructure parameters.

## ACKNOWLEDGMENTS

This work has been supported by Fundação de Amparo à Pesquisa do Estado de São Paulo (FAPESP) and by Conselho Nacional de Desenvolvimento Científico e Tecnológico (CNPq).

## APPENDIX: MATRIX ELEMENTS OF THE 8×8 k·p KANE-WEILER HAMILTONIAN IN PRESENCE OF AN EXTERNAL MAGNETIC FIELD

In presence of an external magnetic field in the $z$ direction, the diagonal elements of the $8\times8$ $\mathbf{k}\cdot\mathbf{p}$ Kane-Weiler Hamiltonian are defined as

$$\hat{D}_{el}^{\pm}=E_g+\left(F+\frac{1}{2}\right)\hat{\mathbf{P}}^2\pm\frac{1}{l_B^2}\left(N_w+\frac{1}{2}\right),$$

$$\hat{D}_{hh}^{\pm}=\hat{D}_{+}\mp\frac{3}{2}\frac{1}{l_B^2}\left(\kappa+\frac{9}{4}q\right),$$

$$\hat{D}_{lh}^{\pm}=\hat{D}_{-}\mp\frac{1}{2}\frac{1}{l_B^2}\left(\kappa+\frac{1}{4}q\right),$$

$$\hat{D}_{\pm}=\left(\frac{\gamma_1\pm\gamma_2}{2}\right)\hat{\mathbf{P}}^2\mp\frac{3}{2}\gamma_2\hat{P}_z^2,$$

$$\hat{D}_{so}^{\pm}=-\Delta_0+\frac{\gamma_1}{2}\hat{\mathbf{P}}^2\mp\frac{1}{l_B^2}\left(\kappa+\frac{1}{2}\right). \tag{A1}$$

The off-diagonal terms are given as

$$\hat{K}_{\pm}=i\sqrt{\frac{1}{6}}P_0\hat{P}'_{\pm},$$

$$\hat{G}_{\pm}=\sqrt{3}\gamma_3\hat{P}'_{\pm}\hat{P}_z,$$

$$\hat{K}_z=i\sqrt{\frac{1}{3}}P_0\hat{P}_z, \tag{A2}$$

$$\hat{W}=\sqrt{3}(\bar{\gamma}\hat{P}'^2_{-}-\mu\hat{P}'^2_{+}),$$

$$\hat{R}_{\pm}=\hat{R}\mp\frac{1}{l_B^2}(\kappa+1),$$

$$\hat{R}=\frac{\sqrt{2}}{2}\gamma_2(\hat{\mathbf{P}}'^2-3\hat{P}_z^2), \tag{A3}$$

where the operators $\hat{P}'_{\pm}$ and $\hat{\mathbf{P}}^2$ in spherical coordinates are given by

$$\hat{P}'_{\pm}=\hat{P}_{\pm}\pm\frac{eB}{2c\hbar}r\sin\theta\exp(\pm i\phi), \tag{A4}$$

$$\hat{\mathbf{P}}^2=\boldsymbol{\nabla}^2+\frac{1}{2l_B^2}\hat{L}_z+\frac{1}{8l_B^4}r^2\sin^2\theta. \tag{A5}$$

Here $\boldsymbol{\nabla}^2$ is the Laplacian operator, $\hat{P}_{\pm}=(\partial/\partial x\pm i\partial/\partial y)$, $\hat{L}_z=-i\partial/\partial\phi$, $\hat{P}_z=\partial/\partial z$, and $\Delta_0$ is the spin-orbit splitting. The additional parameters are defined as

$$\bar{\gamma}=\frac{1}{2}(\gamma_2+\gamma_3),$$

$$\mu=\frac{1}{2}(\gamma_2-\gamma_3).$$

The second-order parameters $F$, $\gamma_1$, $\gamma_2$, and $\gamma_3$ associated with the electron and hole effective mass, respectively, consider the contributions of the remote bands. The parameter $N_w$ ($\kappa$) takes into account the contributions of the remote bands to the conduction (valence) $g$ factor and the $q$ parameter related to the spin-orbit splitting. All the second-order Kane-Luttinger-Weiler parameters $(F+\frac{1}{2})$, $(N_w+\frac{1}{2})$, $\gamma_i$, $(\kappa+\frac{1}{2})$, and $q$ are measured in units of $\hbar^2/m_0$. Also, $P_0=i(\hbar/m_0)\langle s|\hat{p}_x|x\rangle$ is the usual first-order Kane parameter (in units meV-Å) or $E_p=(2m_0/\hbar^2)P_0^2$ (meV), which sets the strength of the conduction valence-band coupling for a give material. We have chosen the sequence $e^+$, $hh^+$, $lh^+$, $so^+$ $e^-$, $hh^-$, $lh^-$, and $so^-$ to represent the conduction, heavy, light, and split-off carriers. The signs ($\pm$) represent the $z$ component of the total angular momentum $\mathbf{J}$ for each carrier.[17] Using the wave function $f_{n,L}^M(r,\Omega)$ introduced in Sec. II, the off-diagonal matrix elements (A2) are given by

$$\langle f_{n',L'}^{M'}|\hat{P}'_{+}|f_{n,L}^{M}\rangle=\frac{1}{R}\delta_{M',M+1}[\delta_{L',L+1}b_{L,M}-\delta_{L',L-1}c_{L,M}]T_{-},$$

$$\langle f_{n',L'}^{M'}|\hat{P}'_{-}|f_{n,L}^{M}\rangle=\frac{1}{R}\delta_{M',M-1}[-\delta_{L',L+1}c_{L+1,M-1}+\delta_{L',L-1}b_{L-1,M-1}]T_{+},$$

$$\langle f^{M'}_{n',L'}|\hat{P}'_z|f^{M}_{n,L}\rangle=\frac{2}{R}\mu^L_n\delta_{n',n}\delta_{M',M}[-a_{L+1,M}\delta_{L',L+1}-a_{L,M}\delta_{L',L-1}]I^{n',n}_{L',L}, \tag{A6}$$

$$\langle f^{M'}_{n',L'}|\hat{P}^{2'}_-|f^{M}_{n,L}\rangle=\delta_{M',M-2}\{\delta_{L',L+2}c_{L+2,M-2}c_{L+1,M-1}B_+ + \delta_{L',L-2}b_{L-2,M-2}b_{L-1,M-1}B_- + \delta_{L',L}[c_{L+1,M-1}b_{L,M-2} + b_{L-1,M-1}c_{L,M-2}]B_0\}, \tag{A7}$$

$$\langle f^{M'}_{n',L'}|\hat{P}^{2'}_z|f^{M}_{n,L}\rangle=\frac{2}{R^2}\mu^L_n\delta_{M',M}I^{n',n}_{L',L}\times[a_{L+1,M}a_{L+2,M}\delta_{L',L+2}(2L+3) - a_{L-1,M}a_{L,M}\delta_{L',L-2}(2L-1)], \tag{A8}$$

$$\langle f^{M'}_{n',L'}|\hat{P}'_+\hat{P}'_z|f^{M}_{n,L}\rangle=\delta_{M',M+1}[a_{L+1,M}b_{L+1,M}\delta_{L',L+2}C_+ + c_{L-1,M}a_{L,M}\delta_{L',L-2}C_- + \delta_{L',L}C_0 \times(-a_{L+1,M}c_{L+1,M}+a_{L,M}b_{L-1,M})], \tag{A9}$$

$$\langle f^{M'}_{n',L'}|\hat{P}'_-\hat{P}'_z|f^{M}_{n,L}\rangle=\delta_{M',M-1}[a_{L+1,M}c_{L+2,M-1}\delta_{L',L+2}D_+ + b_{L-2,M-1}a_{L,M}\delta_{L',L-2}D_- + \delta_{L',L}C_0 \times(-a_{L+1,M}b_{L,M-1}-a_{L,M}c_{L,M-1})], \tag{A10}$$

where

$$T_\pm=\left[2\mu^L_nI^{n',n}_{L',L}\pm\left(\frac{R}{l_B}\right)^2\frac{\tilde{T}^{n',n}_{L',L}(3)}{j_{L+1}(\mu^L_n)j_{L'+1}(\mu^{L'}_{n'})}\right],$$

$$B_\pm=\left\{2\mu^L_n\left[\pm I^{n',n}_{L',L}\frac{2(L\pm1)+1}{R^2} + \frac{1}{l_B^2}\frac{\tilde{T}^{n',n}_{L',L+1}(3)}{j_{L+1}(\mu^L_n)j_{L'+1}(\mu^{L'}_{n'})}\right] + \frac{1}{2}\left(\frac{R}{l_B^2}\right)^2\frac{\tilde{T}^{n',n}_{L',L}(4)}{j_{L+1}(\mu^L_n)j_{L'+1}(\mu^{L'}_{n'})}\right\}, \tag{A11}$$

$$B_0=\left\{-\frac{2\mu^L_n}{l_B^2}\frac{\tilde{T}^{n',n}_{L',L+1}(3)}{j_{L+1}(\mu^L_n)j_{L'+1}(\mu^{L'}_{n'})} - \frac{1}{2}\left(\frac{R}{l_B^2}\right)^2\frac{\tilde{T}^{n',n}_{L',L}(4)}{j_{L+1}(\mu^L_n)j_{L'+1}(\mu^{L'}_{n'})}\right\},$$

$$C_\pm=-2\mu^L_n\left\{I^{n',n}_{L',L}\left[\frac{2(L\pm1)+1}{R^2} \pm\frac{1}{l_B^2}\frac{\tilde{T}^{n',n}_{L',L+1}(3)}{j_{L+1}(\mu^L_n)j_{L'+1}(\mu^{L'}_{n'})}\right]\right\}, \tag{A12}$$

$$D_\pm=+2\mu^L_n\left\{I^{n',n}_{L',L}\left[\frac{2(L\pm1)+1}{R^2} \pm\frac{1}{l_B^2}\frac{\tilde{T}^{n',n}_{L',L+1}(3)}{j_{L+1}(\mu^L_n)j_{L'+1}(\mu^{L'}_{n'})}\right]\right\}, \tag{A13}$$

$$C_0=\frac{\mu^L_n}{l_B^2}\frac{\tilde{T}^{n',n}_{L',L+1}(3)}{j_{L+1}(\mu^L_n)j_{L'+1}(\mu^{L'}_{n'})},$$

$$a_{L+1,M}=\sqrt{\frac{(L-M+1)(L+M+1)}{(2L+1)(2L+3)}},$$

$$b_{L,M}=\sqrt{\frac{(L+M+2)(L+M+1)}{(2L+1)(2L+3)}},$$

$$c_{L,M}=\sqrt{\frac{(L-M)(L-M-1)}{(2L-1)(2L+1)}}. \tag{A14}$$

The overlap integrals are given by

$$I^{n',n}_{L',L}=\frac{\mu^{L'}_{n'}}{(\mu^{L'}_{n'})^2-(\mu^L_n)^2}. \tag{A15}$$

$$\tilde{T}^{n',n}_{L',L}(p)=\int_0^1 j_{L'}(\mu^{L'}_{n'}x)x^pj_L(\mu^L_nx)dx. \tag{A16}$$

*Electronic address: psprado@df.ufscar.br

[1] J. Planelles, W. Jaskólski, and J. Aliaga, Phys. Rev. B **65**, 033306 (2002).
[2] R. Rinaldi, P. V. Giugno, R. Cingolani, F. Rossi, E. Molinari, U. Marti, and F. K. Reinhart, Phys. Rev. B **53**, 13 710 (1996).
[3] W. Heller and U. Brockelmann, Phys. Rev. B **55**, R4871 (1997).
[4] N. Miura, Y. H. Matsuda, K. Uchida, and H. Arimoto, J. Phys.: Condens. Matter **11**, 5917 (1999).
[5] M. Bayer, A. Schmidt, A. Forchel, and F. Faller, Phys. Rev. Lett. **74**, 3439 (1999).
[6] S. Nomura, Y. Segawa, K. Misawa, T. Kobayashi, X. Zhao, Y. Aoyagi, and T. Sugano, J. Lumin. **70**, 144 (1996).

[7] Z. Xiao, J. Appl. Phys. **86**, 4509 (1999).
[8] R. Kotlyar, T. L. Reinecke, M. Bayer, and A. Forchel, Phys. Rev. B **63**, 085310 (2001).
[9] P. A. Knipp and T. L. Reinecke, Phys. Rev. B **54**, 1880 (1996).
[10] T. Darnhofer and U. Rössler, Phys. Rev. B **47**, 16 020 (1993).
[11] H. X. Jiang, Phys. Rev. B **35**, 9287 (1987).
[12] A. M. Alcalde and G. E. Marques, Phys. Rev. B **65**, 113301 (2002).
[13] J. Planelles, J. G. Díaz, J. Climente, and W. Jaskólski, Phys. Rev. B **65**, 245302 (2002).
[14] E. O. Kane, J. Phys. Chem. Solids **1**, 249 (1957).
[15] M. H. Weiler, *Magnetooptical Properties of* $Hg_{1-x}Cd_xTe$ *Alloys*, Vol. 16 of *Semiconductor and Semimetals*, 1st ed. (Academic, New York, 1981), Chap. 3, pp. 119–191.
[16] V. López-Richard, Ph.D. thesis, Universidade Federal de São Carlos, 2001.
[17] V. López-Richard, G. E. Marques, and C. Trallero-Giner, Phys. Status Solidi B **231**, 263 (2002).
[18] $A_{n,l}$ is the normalization constant and $\alpha_{n,l}$ is the $n$th zero of the $l$-order spherical Bessel function $j_l(x)$.
[19] The generalization to other matching boundary conditions as the continuity of the current through the quantum dot surface is straightforward.
[20] A. L. Efros and M. Rosen, Phys. Rev. B **58**, 7120 (1998).